



# Large uncertainties in global hydroxyl projections tied to fate of reactive nitrogen and carbon

Lee T. Murray<sup>a,1</sup>, Arlene M. Fiore<sup>b,c,2</sup>, Drew T. Shindell<sup>d</sup>, Vaishali Naik<sup>e</sup>, and Larry W. Horowitz<sup>e</sup>

<sup>a</sup>Department of Earth and Environmental Sciences, University of Rochester, Rochester, NY 14627; <sup>b</sup>Department of Earth and Environmental Sciences, Columbia University, New York, NY 10027; <sup>c</sup>Lamont-Doherty Earth Observatory, Columbia University, Palisades, NY 10964; <sup>d</sup>Nicholas School of the Environment, Duke University, Durham, NC 27708; and <sup>e</sup>Geophysical Fluid Dynamics Laboratory, National Oceanic and Atmospheric Administration, Princeton, NJ 08540

Edited by Mark Thieme, University of California San Diego, La Jolla, CA, and approved September 22, 2021 (received for review August 18, 2021)

**The hydroxyl radical (OH) sets the oxidative capacity of the atmosphere and, thus, profoundly affects the removal rate of pollutants and reactive greenhouse gases. While observationally derived constraints exist for global annual mean present-day OH abundances and interannual variability, OH estimates for past and future periods rely primarily on global atmospheric chemistry models. These models disagree  $\pm 30\%$  in mean OH and in its changes from the preindustrial to late 21st century, even when forced with identical anthropogenic emissions. A simple steady-state relationship that accounts for ozone photolysis frequencies, water vapor, and the ratio of reactive nitrogen to carbon emissions explains temporal variability within most models, but not intermodel differences. Here, we show that departure from the expected relationship reflects the treatment of reactive oxidized nitrogen species ( $\text{NO}_y$ ) and the fraction of emitted carbon that reacts within each chemical mechanism, which remain poorly known due to a lack of observational data. Our findings imply a need for additional observational constraints on  $\text{NO}_y$  partitioning and lifetime, especially in the remote free troposphere, as well as the fate of carbon-containing reaction intermediates to test models, thereby reducing uncertainties in projections of OH and, hence, lifetimes of pollutants and greenhouse gases.**

hydroxyl | atmospheric oxidative capacity | forecasting change

The hydroxyl radical (OH) is a keystone chemical species in the atmosphere, determining the removal rate of many trace gases of importance to climate, composition, and human and ecosystem health (1). For example, reaction with OH in the troposphere\* is the dominant sink for methane, a powerful greenhouse gas and precursor for tropospheric ozone, a major surface pollutant and greenhouse gas itself (2). Understanding what drives variability in OH is therefore critical for forecasting future changes in the self-cleansing capability of the atmosphere. The fundamental chemistry of background OH has been well known for decades (3–5). Nevertheless, global atmospheric chemistry models show large disagreement in mean OH and its transient response to specified changes in emissions (6, 7).

Fig. 1 shows global mean OH and its temporal evolution within the ensemble of simulations that participated in the Atmospheric Chemistry-Climate Model Intercomparison Project (ACCMIP) (8). The ACCMIP ensemble is a comprehensive suite of global three-dimensional atmospheric chemistry models driven by identical anthropogenic emission scenarios for the period 1850–2100 (9, 10). Despite applying identical anthropogenic emissions in all ACCMIP models, tropospheric mean abundances of OH range  $\pm 30\%$  relative to the multimodel mean during the last decade of the historical simulation (gray-shaded interval of Fig. 1). The models also disagree as to whether OH increases or decreases across any prescribed emission scenario, except for a small window between 1980 and 2010 (when all increase).

\*The troposphere is the lowermost several kilometers of the atmosphere in contact with the Earth's surface.

Our best estimates of global mean abundance and interannual variability from OH rely on proxy measurements, particularly methyl chloroform (11), as the high reactivity and short lifetime of OH make direct measurement difficult and impractical for constraining spatial and temporal variability (12). On average, global atmospheric chemistry models cannot reproduce meridional gradients in carbon monoxide (CO) and other long-lived reactants, implying possible errors in simulated OH spatial and seasonal distributions (6, 13). They also overestimate global mean OH with respect to observational constraints from the methane and methyl chloroform lifetimes (6, 7) and underestimate the magnitude of interannual variability in OH inferred from proxy observations [ $0.5 \pm 0.4\%$  of year-to-year changes in the ACCMIP ensemble versus  $2.3 \pm 1.5\%$  derived from methyl chloroform (11)]. These findings highlight gaps in our understanding of the processes that determine the oxidative capacity of the atmosphere and its variability, thereby hindering our ability to accurately predict its future evolution.

In contrast to the intermodel discrepancies in OH abundances, trends, and variability, the models tend to produce consistent simulations for key tropospheric species that are intimately coupled with OH, such as tropospheric ozone (14). This implies that some—or even all—models are capturing mean abundances and spatial and temporal trends of longer-lived species at least partly for the wrong reasons.

## Significance

Reaction with the hydroxyl radical (OH) is the dominant loss mechanism for many atmospheric gases of interest for air quality, climate change, and stratospheric ozone. Understanding how and why OH may change in the future is therefore paramount for predicting changes in the societal impacts associated with such changes. Future models' projections strongly disagree in how OH responds to changing emissions and climate—even in the sign. Here, we demonstrate that intermodel differences in OH are best explained by disparate implementations of chemical and physical processes that affect reactive oxides of nitrogen and organic chemical species. Targeted observations can reduce uncertainty in the chemical budgets of these key species to increase confidence in future projections of composition and its impacts.

Author contributions: L.T.M. designed research; L.T.M. performed research; L.T.M. analyzed data; and L.T.M., A.M.F., D.T.S., V.N., and L.W.H. wrote the paper.

The authors declare no competing interest.

This article is a PNAS Direct Submission.

Published under the PNAS license.

<sup>1</sup>To whom correspondence may be addressed. Email: lee.murray@rochester.edu.

<sup>2</sup>Present address: Department of Earth, Atmospheric, and Planetary Sciences, Massachusetts Institute of Technology, Cambridge, MA 02139.

This article contains supporting information online at <https://www.pnas.org/lookup/suppl/doi:10.1073/pnas.2115204118/-DCSupplemental>.

Published October 22, 2021.

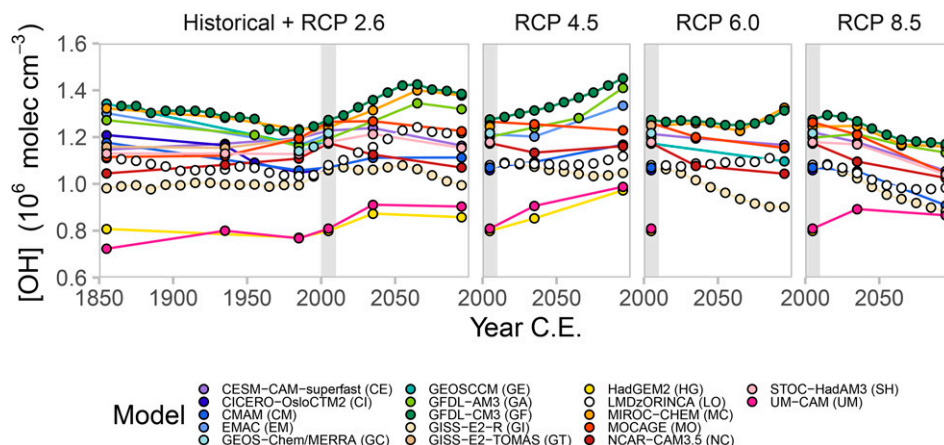


**Fig. 1.** Large disagreement in decadal mean tropospheric OH and its transient evolution in global atmospheric chemistry models. The models shown prescribe identical anthropogenic emissions from a historical reconstruction (9) and four possible future RCP scenarios (10). Different colors represent different models. The gray rectangle highlights the period 2000 to 2010 in each scenario. Full model names are shown in the key, with a two-letter abbreviation shown in parentheses used in subsequent figures.

The original analysis of OH in the ACCMIP simulations noted that the change in OH over time in a given model correlated with the ratio of change in its burden of reactive nitrogen oxides ( $\text{NO}_x \equiv \text{NO} + \text{NO}_2$ ) to change in its CO burden, but did not provide a mechanistic explanation (6). Here, we reexamine the ACCMIP model ensemble through the lens of fundamental OH chemistry to explain the disparate behavior between the models. The key areas of uncertainty we identify provide a target for future observing strategies to advance most rapidly our understanding, as formalized in the models used to project future atmospheric abundances of pollutants and reactive greenhouse gases.

### A Steady-State Relationship for OH

The key reactions controlling OH are highly and nonlinearly coupled to one another (refs. 3–5 and *SI Appendix, Fig. S1*). In the GEOS-Chem chemistry-transport model (CTM; *Materials and Methods*), primary production of OH by photolysis or photolysis-initiated chains contributes to ~60% of total production in the present day, with most of that source resulting from photolysis of ozone in the presence of water vapor. The remaining 40% results from chemical recycling of the  $\text{HO}_x$  family ( $\text{HO}_x \equiv \text{OH} + \text{peroxy radicals}$ ) via reaction of peroxy radicals with reactive oxides of nitrogen ( $\text{NO}_x$ ) or ozone. Loss of OH is primarily via reaction with reduced carbon species, such as CO (40%) and methane (15%), with products of methane oxidation, other nonmethane volatile organic compounds (NMVOCs) and their oxidation products, ozone,  $\text{H}_2$ ,  $\text{HO}_x$  species, and other minor species accounting for the remainder. Here, we refer to the sum of CO, methane and, all NMVOCs as total “reactive carbon.”

The equations that describe the dominant OH photochemistry are simple enough that they yield an analytic solution for OH when one assumes “steady state,” in which the sum of the source terms is balanced by all loss terms (*SI Appendix, section 1*). At steady state, variations in OH should vary proportional to

$$J_{\text{O}(^1D)} q \frac{S_N}{S_C}, \quad [1]$$

where  $J_{\text{O}(^1D)}$  is the photolysis frequency of ozone to  $\text{O}(^1D)$  ( $\text{s}^{-1}$ ),  $q$  is the specific humidity ( $\text{kg H}_2\text{O kg air}^{-1}$ ), and  $S_N$  and  $S_C$  are the emission rates of  $\text{NO}_x$  ( $\text{Tmol N y}^{-1}$ ) and reactive carbon ( $\text{Tmol C y}^{-1}$ ) species, respectively. The first two terms limit the rate of total  $\text{HO}_x$  production, whereas

the emission ratio determines the relative partitioning of  $\text{HO}_x$  between OH and peroxy radicals (with nitrogen oxides favoring OH and reactive carbon favoring peroxy radicals). The exponent in the denominator accounts for nonlinear feedbacks in the coupled chemistry. Collectively, the relationship describes how the basic OH photochemistry changes in response to changing emissions and climate parameters. Eq. 1 has been used to explain global OH variability within a single CTM across a wide range of climate and emissions scenarios with high skill (15). However, in principle, it should hold across multiple models, as it derives from the analytic solution to the steady-state OH photochemistry.

Large temporal and intermodel variability exists within the decadal mean evolution of each component of Eq. 1 of the ACCMIP ensemble (*SI Appendix, Fig. S2*). The models employed a variety of methods for determining photolysis rates, ranging from look-up tables to online calculation with column radiation codes (8). Most models agree in their mean photolysis frequencies, although outliers exist in the ensemble. Changes in photolysis frequencies with time are relatively small compared to intermodel variability, although it has been shown that OH is especially sensitive to them (e.g., refs. 15–17). These temporal changes are driven primarily by changes in overhead ozone abundances associated with anthropogenic emissions of stratospheric ozone-depleting substances and greenhouse gases (18), with peak photolysis rates in each model occurring during the height of stratospheric ozone loss circa 1980–2010. The models are in tight agreement in both tropospheric mean water-vapor abundance and its exponential increase over time in response to temperature-driven increases in saturation water-vapor pressure (19).  $\text{NO}_x$  emissions are dominated by the prescribed anthropogenic sources, and, therefore, temporal variability dominates over intermodel variability. However, slight differences do exist between models and in time due to different parameterizations of climate-sensitive natural sources, such as lightning (20). In contrast, emissions of reactive carbon species vary widely across the models and in time. These variations are dominated by natural sources; the models employed a wide range of biogenic NMVOC implementations with respect to species emitted (including none), chemical mechanism, base emissions, and the response of emissions to changes in meteorology, e.g., the increase in isoprene emission by terrestrial plants at warmer temperatures (21).

Fig. 2 shows decadal mean OH in the ACCMIP simulations as a function of Eq. 1. If differences in the four key parameters in *SI Appendix, Fig. S2* were sufficient to explain OH variability within and between the models, then all points would fall on the

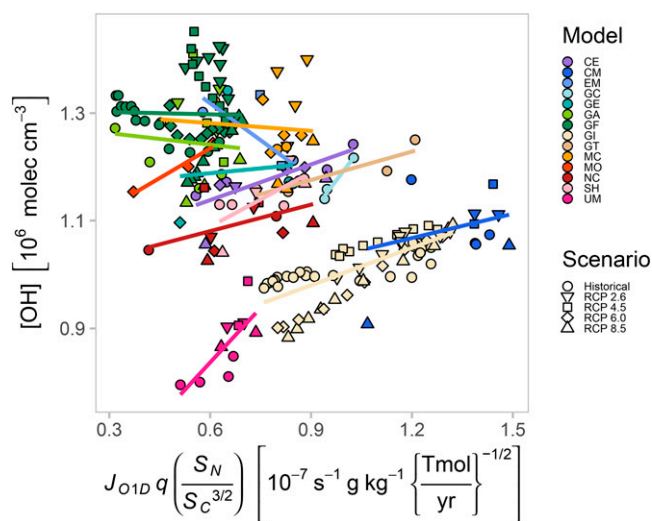


**Fig. 2.** Decadal mean OH as a function of the steady-state photochemical relationship. Variability within many individual models is accurately explained by Eq. 1. However, large intermodel variability is not. Individual models are identified by color and emission scenario by shape. An ordinary linear regression line is shown for each model subpopulation. See *SI Appendix, Fig. S3* for individual model detail at annual time scales.

same line with a positive slope. The OH steady-state predictor is usually sufficient to explain variability within individual models, although not in the models with the highest mean OH abundances. A large mode of residual intermodel variability dominates the ensemble variability. This intermodel variability lies largely orthogonal to that explained by the OH photochemistry and is therefore likely independent.

Fig. 3 shows that the residual variability can be best explained by considering two parameters derived from available ACCMIP model diagnostics. First, the large intermodel variability is primarily related to the NMVOC “oxidation efficiency,”  $\epsilon_C$ , which we define as the fraction of carbon atoms emitted in NMVOC compounds oxidized to CO before removal from the atmosphere (units of mol C per mol C). Models that have a higher fraction of their emitted carbon converted to CO tend to have lower OH (Fig. 3A). Second, departure from linearity within a single model

is primarily related to shifts in the tropospheric lifetime of  $\text{NO}_x$ ,  $\tau_{\text{NO}_x}$  (units of time; Fig. 3B). Variations in these two parameters act to alter the magnitude of the  $\text{HO}_x$  partitioning response to changes in emissions of  $\text{NO}_x$  versus reduced carbon species in Eq. 1.

### Factors Driving Model Diversity

The most apparent correlation of intermodel variability in Fig. 3 is with the NMVOC oxidative efficiency ( $\epsilon_C$ ), with models having higher  $\epsilon_C$  tending to have lower OH. While the greatest sinks of OH are CO and methane, respectively, these do not vary much between the ACCMIP models by design; methane and anthropogenic CO are prescribed, and nearly all methane is oxidized to CO (22). The large intermodel variability in NMVOC emissions is not correlated with intermodel variability in global mean OH, even though NMVOCs consume OH, because relatively short NMVOC lifetimes restrict their influence to be immediately downwind of sources, which are mostly in the continental boundary layer. Instead, differences in the portion of NMVOCs fully oxidized to CO (i.e.,  $\epsilon_C$ ), a gas with a sufficiently long lifetime to mix into the free and remote troposphere, best explain intermodel variability in global mean OH.

From the perspective of reactive carbon, the atmosphere is a low-temperature furnace: Reduced organic gases are emitted and subsequently oxidized through a chain of increasingly semioxidized species toward CO and  $\text{CO}_2$ . However, increased oxidation tends toward lower-volatility species that may condense (23). Other intermediates are soluble and/or prone to surface uptake, and physical processes may siphon these from the atmosphere as well. All in all, physical loss is a greater atmospheric sink of NMVOC carbon than chemical conversion to CO and  $\text{CO}_2$  in most models ( $\epsilon_C$  often  $<0.5$ ; Fig. 3A and *SI Appendix, Fig. S4*; also refs. 24–26).

Atmospheric model developers must make choices that influence an individual model’s oxidative efficiency. We must balance a yet-imperfect scientific understanding of atmospheric oxidation mechanisms (e.g., ref. 27) with desired model capabilities and computational limitations. Near-explicit mechanisms using elementary reactions based on observational constraints for the oxidation of isoprene alone would require thousands of reactions and several hundred species (28), intractable for global atmospheric models. For these reasons, global models typically employ reduced chemical mechanisms with lumped surrogate

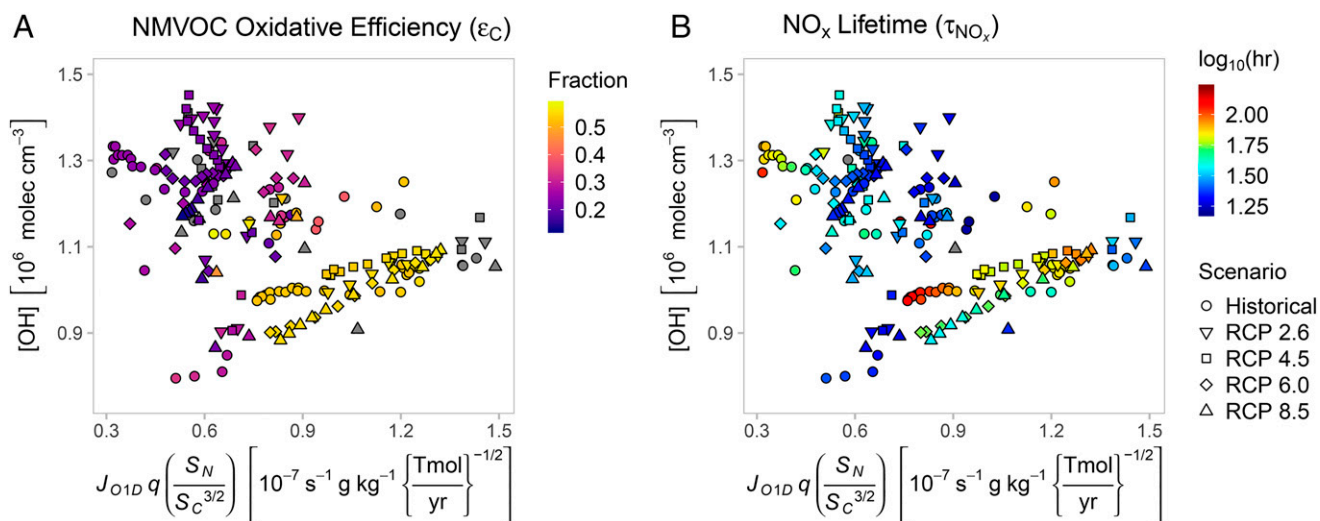


**Fig. 3.** Residual intermodel and intramodel variability of Fig. 2 explained by two parameters. (A) The points of Fig. 2 colored by their decadal mean “oxidative efficiency,” the fraction of emitted NMVOC carbon that is oxidized to CO before atmospheric removal. (B) The points colored by  $\tau_{\text{NO}_x}$ , i.e., the  $\text{NO}_x$  burden ( $\equiv \text{NO} + \text{NO}_2$ ) divided by its source. Gray-shaded points indicate insufficient model data archived for calculation.

species and empirically derived stoichiometries in order to best reproduce observations within computational limits.

We highlight two end members of the ACCMIP ensemble by contrasting the hydrocarbon oxidation mechanisms of the Goddard Institute for Space Studies (GISS) and Geophysical Fluid Dynamics Laboratory (GFDL) models. In the GISS model (SI Appendix, Fig. S5), gaseous NMVOCs are emitted as 2 explicit and 3 lumped species, transforming among 18 NMVOC species before conversion to CO. All oxidation pathways lead to CO, except for 7 species (39%) that may be physically removed and a terminal pathway included to enable tuning of relative oxidation rates to observations (29). In contrast, the GFDL model (SI Appendix, Fig. S6) emits NMVOCs as 10 explicit and 2 lumped species and transforms among 44 total NMVOC species, with 28 species (64%) physically removable by wet or dry processes. Furthermore, the GFDL empirical oxidation stoichiometries include partial direct conversion of NMVOCs to CO<sub>2</sub>, bypassing CO. Given the greater opportunity for loss of intermediates, only 23% of NMVOC emitted by the GFDL model is oxidized to CO, versus 53% in the GISS model. Consequently, the GISS model has a greater fraction of its emitted reactive carbon reacting with OH and, thereby, lower OH.

Despite large intermodel variability, the oxidative efficiency is relatively invariant in time for a given model (SI Appendix, Fig. S7). This implies that the oxidative efficiency is primarily determined by the specific combination of species, reactions, and sinks implemented in a given model. Nevertheless, minor temporal changes occur, reflecting shifts in the distribution and magnitudes of reactive carbon emissions and precipitation. For example, the methane increase in the “Representative Concentration Pathway” (RCP) 8.5 scenario consumes a larger fraction of OH, slowing the oxidation rate of NMVOCs, allowing more time for intermediate species to be lost via deposition, thereby reducing  $\epsilon_C$  in some models.

In contrast to  $\epsilon_C$ , variability in  $\tau_{NO_x}$  contributes to both intermodel and intramodel variability in OH. The rapid cycling of NO<sub>x</sub> between NO and NO<sub>2</sub> allows for the catalytic production of relatively large quantities of OH (SI Appendix, Fig. S8); otherwise, all OH would be quickly titrated from the atmosphere. Longer  $\tau_{NO_x}$  enables relatively more OH production per NO<sub>x</sub> molecule. Global mean  $\tau_{NO_x}$  varies by orders of magnitude across models (Fig. 3B), and some models simulate temporal changes by nearly as much, although others suggest little change (SI Appendix, Fig. S7). Therefore, variations in  $\tau_{NO_x}$  can influence both intermodel and intramodel changes in global mean OH. SI Appendix, Fig. S9 demonstrates the sensitivity of the steady-state OH abundance to mean  $\tau_{NO_x}$  in the GFDL model. The factors controlling the lifetime of NO<sub>x</sub> are many

and can compete in sign. We next demonstrate the sensitivity of global mean OH to three key parameters with known intermodel disparities.

First, the ACCMIP models employ very different vertical and meridional distributions of lightning NO<sub>x</sub> (cf. figure 3 of ref. 20). Because  $\tau_{NO_x}$  increases exponentially with altitude, global mean  $\tau_{NO_x}$  is highly sensitive to the mean vertical injection height of lightning NO<sub>x</sub>. Most models release lightning NO<sub>x</sub> into the free troposphere. However, two ACCMIP ensemble members (UM and HG; see Fig. 1 for definitions of abbreviations) release their lightning NO<sub>x</sub> primarily into the boundary layer. When we compare a sensitivity simulation using the GEOS-Chem CTM with lightning NO<sub>x</sub> released at the surface instead of at altitude, global mean OH decreases by 22% (Fig. 4A), a sizable portion of the difference in OH between GEOS-Chem and the two ACCMIP models releasing all lightning NO<sub>x</sub> near the surface (Fig. 4D).

Second, heterogeneous reactions can vary substantially between global models. Uptake of gaseous species on the surface of aerosol particles is a highly efficient means for sequestering NO<sub>y</sub> and HO<sub>x</sub> from the atmosphere, short-circuiting the OH photochemistry included in Eq. 1. Most models include hydrolysis of N<sub>2</sub>O<sub>5</sub> on aerosol particles, often the dominant local sink for NO<sub>y</sub>, with a known strong influence on global OH (30, 31). However, models differ in implementation (e.g., some models vary the uptake coefficient  $\gamma$  with aerosol composition), as well as in the inclusion of other heterogeneous losses. When we disable heterogeneous losses within GEOS-Chem [normally N<sub>2</sub>O<sub>5</sub> hydrolysis with  $\gamma_{N_2O_5} \leq 0.02$  (32) and HO<sub>2</sub> uptake with  $\gamma_{HO_2} \leq 0.1$  (33)], global mean OH increases by 12% (Fig. 4B), the magnitude of many intermodel differences. We note that the only difference in the gas-phase chemistry of the two variants of the GISS model submitted to the ACCMIP study was that one included heterogeneous uptake of HNO<sub>3</sub> on dust particles (GI; ref. 34) and one did not (GT), resulting in a longer  $\tau_{NO_x}$  and 20% higher OH in the latter (Fig. 4D).

Lastly, NO<sub>y</sub> is often stored in relatively long-lived reservoir species, which prolong and redistribute the influence of NO<sub>x</sub> on oxidants. However, these reservoir species may also be lost to deposition, which bypasses the assumption that all NO<sub>x</sub> is lost via oxidation to HNO<sub>3</sub> intrinsic to Eq. 1. One particular area of model diversity in NO<sub>y</sub> reservoirs regards the fate of isoprene nitrates, products of oxidation of isoprene by NO<sub>x</sub>, especially at night. Some chemical mechanisms, including that implemented in our version of GEOS-Chem, assume that this nitrate is immediately lost to deposition, reflecting observational evidence that this can be a major local NO<sub>y</sub> sink (e.g., ref. 35). Others allow for part of this nitrate to be recycled back to NO<sub>x</sub>. When we perform

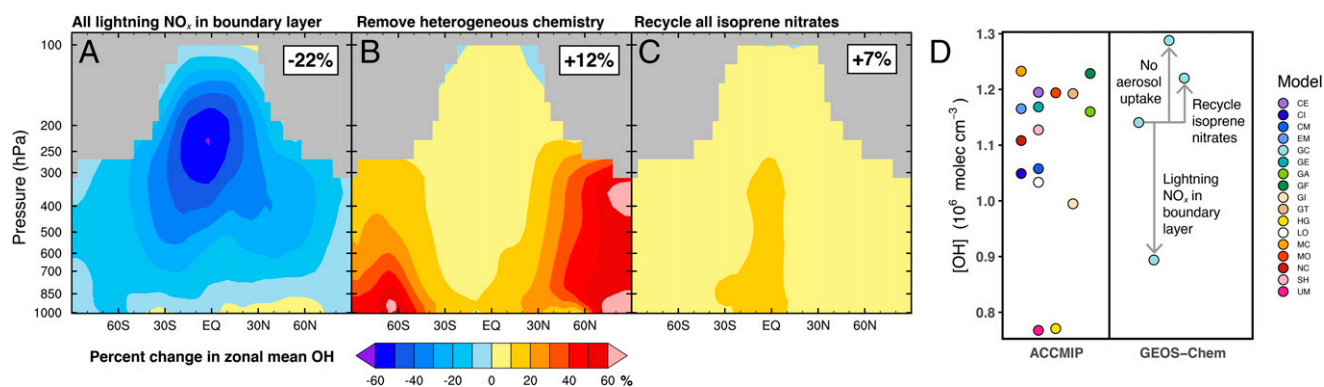


**Fig. 4.** Global mean OH is highly sensitive to the treatment of reactive nitrogen. (A–C) Change in zonal mean OH in the GEOS-Chem CTM for the year 1980 for the following scenarios: All lightning NO<sub>x</sub> is released into the planetary boundary layer instead of at altitude (A); all heterogeneous reactions are turned off (B); and all nitrogen sequestered in isoprene nitrates is recycled back to NO<sub>x</sub> (C). The box reports the percent change in the global OH burden. (D) Decadal mean OH in the ACCMIP models for the 1980s versus that in GEOS-Chem and the three sensitivity simulations shown in A–C. The x axis is arbitrary.

a sensitivity test in GEOS-Chem, in which we allow all isoprene nitrates to be recycled back to  $\text{NO}_x$ , global mean OH increases by 7% (Fig. 4C), the magnitude of differences between GEOS-Chem and the GFDL model (GA and GF), which included isoprene nitrate recycling (albeit <100%; ref. 36).

Disparate implementations of processes that affect  $\tau_{\text{NO}_x}$  therefore cause the  $\text{NO}_y$  budget to be a key source of model uncertainty with respect to OH. Fig. 5 shows that despite nearly identical  $\text{NO}_x$  emission magnitudes, the models show large variability in their absolute burdens and relative partitioning of the dominant  $\text{NO}_y$  species. This is much greater than seen in the longer-lived species, such as ozone and CO. Furthermore, Fig. 5 is missing other major  $\text{NO}_y$  species not archived for ACCMIP, e.g., HONO or  $\text{HO}_2\text{NO}_2$ , which likely also vary between models.

Taken together, the sensitivity of global mean OH to  $\epsilon_C$  and  $\tau_{\text{NO}_x}$  implies that a key assumption of Eq. 1 does not hold between models or within some models, i.e., the sources of reactive nitrogen and carbon are not balanced by their dominant sinks with respect to OH (oxidation to nitric acid and carbon dioxide, respectively). Various processes siphon emitted reactive nitrogen and carbon from the atmosphere before they may influence OH photochemistry. It is variations in the fraction of total nitrogen and carbon loss pathways that involve OH that ultimately control OH abundance in the models and, therefore, the atmospheric chemistry and physics that occur between emission and loss. Fig. 6 shows that we are better able to capture intermodel and intramodel variability in OH by shifting our focus from the sources of nitrogen and carbon to the sinks ( $R = 0.5$  for  $n = 221$  decadal time slices).

## Conclusions

Atmospheric chemistry model contributions to the ACCMIP experiment strongly disagree in their global mean OH and its transient evolution in response to prescribed changes in anthropogenic emissions (Fig. 1). A steady-state relationship derived from the basic coupled photochemistry of the  $\text{O}_x\text{-HO}_x\text{-NO}_x\text{-CO}$  system explains OH variability within models if the  $\text{NO}_x$  lifetime ( $\tau_{\text{NO}_x}$ ) remains relatively constant (Fig. 2). However, model OH is sensitive to intermodel differences in the fraction of nonmethane volatile organic carbon that is completely oxidized through CO (and  $\text{CO}_2$ ),  $\epsilon_C$ , as well as  $\tau_{\text{NO}_x}$  (Fig. 3). The oxidative efficiency is generally fixed for a given model, determined by the kinetics of the reactions and species included in the model. In contrast, the  $\text{NO}_x$  lifetime is much more variable between models, and even within some models, and is especially sensitive to the altitude of lightning emissions, heterogeneous chemistry, and treatment of reactive nitrogen reservoir species (Fig. 4), although this list is not exhaustive. Variations in global mean OH between

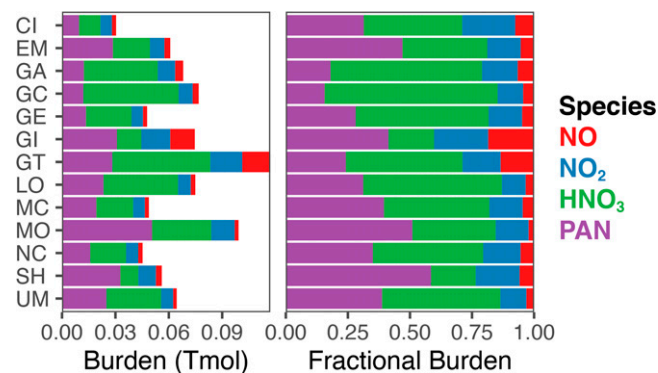


**Fig. 5.** ACCMIP models show large disagreement in their reactive nitrogen budgets. (Left) The cumulative absolute burdens of the four dominant  $\text{NO}_y$  species: peroxyacetyl nitrate (PAN),  $\text{HNO}_3$ ,  $\text{NO}_2$ , and NO. Decadal tropospheric mean is shown for the 2000s from 13 global atmospheric chemistry models. (Right) The cumulative fractional burdens per model.

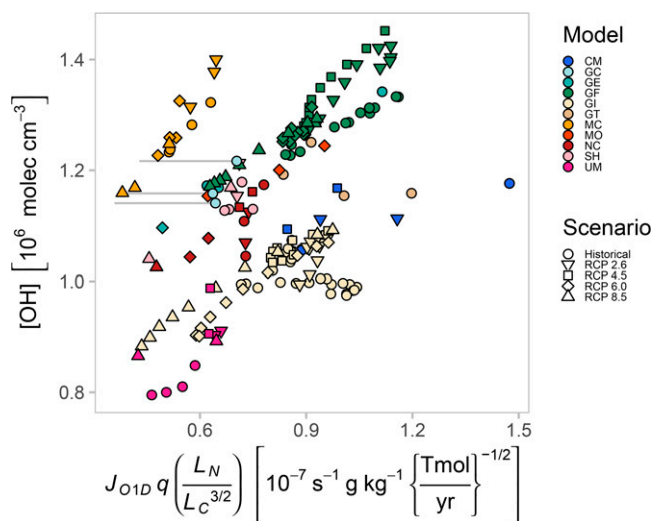


**Fig. 6.** Variability in decadal mean OH in the ACCMIP simulations is better captured when considering photochemical sinks of reactive nitrogen and carbon (as in this figure) than sources (as in Fig. 2). Instead of emission, we apply the total loss rate of CO and methane ( $L_C$ ), which is equivalent to the sum of the sources of CO, methane, and the oxidative efficiency times the NMVOC source. Furthermore, we estimate the loss of  $\text{NO}_x$  to nitric acid ( $L_N$ ). See *Materials and Methods* for details. Gray horizontal lines indicate the error in estimating  $L_N$  from archived monthly mean values relative to online calculation with GEOS-Chem (not archived by the ACCMIP experiment).

and within global models are therefore better characterized by variations in the relative loss pathways of reactive nitrogen and carbon than in their emissions (Fig. 6).

We recommend that future efforts diagnose complete reactive nitrogen budgets in models, especially in the tropical free troposphere. Evaluating these simulated budgets requires comprehensive new measurements that expand beyond the recent NASA Atmospheric Tomography mission, the most extensive global in situ dataset to date (37). Likewise, we recommend that future observational campaigns target quantification of the global source of CO from NMVOC oxidation. Improved observational estimates of  $\tau_{\text{NO}_x}$  and  $\epsilon_C$  will help to constrain models and improve projections of the future oxidizing power of the atmosphere.

## Materials and Methods

**Data Analyzed.** The ACCMIP consisted of 16 atmospheric chemistry models driven by identical anthropogenic emissions and climate forcings over the 1850–2100 period (8). Most models were run as decadal time-slice experiments for a few core decades (1850s, 1980s, 2000s, 2030s, and 2090s), although the GISS-E2-R model submitted its transient simulations for the Coupled Model Intercomparison Project Phase 5 (CMIP5). The ACCMIP and CMIP5 simulations were performed in support of the Fifth Assessment Report of the Intergovernmental Panel on Climate Change. The diagnostics saved for the ACCMIP study are archived at the British Atmospheric Data Centre (<https://archive.ceda.ac.uk/>), as downloaded in September 2019. Here, we analyze the historical simulations and the four future RCP scenarios (10). All 3-d and 2-d variables were processed at monthly temporal resolution by integrating tropospheric totals or airmass-weighted mean values, as appropriate. The troposphere is defined with a mass chemical tropopause of 150 parts per billion by volume ozone, consistent with earlier ACCMIP analyses (6, 7, 14). The monthly values are then averaged to obtain decadal means. We supplement the ACCMIP data with transient runs from the GFDL-CM3 contribution to the CMIP5 study that used the same emissions and forcings (38) and GEOS-Chem (*Original Simulation Description*).

Ozone photolysis is directly archived (*photo1d*) or estimated from the archived OH production rate (*prodohj3*) using coefficients from the Jet Propulsion Laboratory Handbook (39). Specific humidity is archived as *hus*.  $S_N$  is archived as *eminox*.  $S_C$  is the sum of total emission of CO (*emico*), NMVOCs (*emivoc*), and methane, which we assume is equivalent to the total loss rate of methane (*lossch4*). Emission totals are adjusted to match

values self-reported by the modeling groups in Lamarque et al. (8), as outlined in *SI Appendix, section S2*. By assuming that direct emissions and chemical production of CO from methane and NMVOCs are balanced by its total chemical loss, then the oxidative efficiency can be estimated as  $\epsilon_C \equiv \frac{P(\text{CO})_{\text{NMVOC}}}{E_{\text{NMVOC}}} \approx \frac{L(\text{CO}) - E_{\text{CO}} - P(\text{CO})_{\text{CH}_4}}{E_{\text{NMVOC}}}$ . Total chemical loss of CO is archived as *lossco*, and, again, we use *emivoc* and *emico*. We estimate the source of CO from methane oxidation by assuming a 100% conversion of oxidized methane from *lossch4* to CO (22).  $\tau_{\text{NO}_x}$  is determined as the total burden of NO (*vmrno*) and NO<sub>2</sub> (*vmrno2*) divided by the total source (*eminox*).

To adjust the steady-state relationship for Fig. 6, we estimate  $L_C$  as *lossco* + *lossch4*, which neglects carbon lost to intermediates. We estimate  $L_N$  as the production rate of HNO<sub>3</sub> from the pressure-dependent NO<sub>2</sub> + OH reaction using monthly archived NO<sub>2</sub>, OH, air density, and temperature and rate constants from ref. 39.

**Original Simulation Description.** We use the default GEOS-Chem global CTM (v9-01-03; available at <http://www.geos-chem.org>) with its "tropchem"

mechanism driven by MERRA reanalysis meteorological fields (40) degraded to 4° latitude by 5° longitude by 47 vertical levels (38 in the troposphere), and the same emissions used in the ACCMIP study. Methane is prescribed as a surface boundary condition and allowed to advect and react, consistent with the ACCMIP models. The base simulation is initialized over the year 1979, and then archived for 1980–2010. NO<sub>x</sub> sensitivity experiments are then performed by reinitializing over 1979 and archiving year 1980 for the three scenarios described in *Factors Driving Model Diversity*.

**Data Availability.** Processed data used in the figures have been deposited in Zenodo (DOI: [10.5281/zenodo.5576887](https://doi.org/10.5281/zenodo.5576887)). All other study data are included in the article and/or supporting information.

**ACKNOWLEDGMENTS.** L.T.M. was supported in part by a NASA Postdoctoral Program fellowship administered by the Universities Space Research Association. A.M.F. was supported by NASA Atmospheric Composition Modeling and Analysis Program Grant NNX17AG40G. D.T.S. was supported by NASA GISS Grant 80NSSC19M0138 and the NASA Center for Climate Simulation.

- D. H. Ehhalt, Photooxidation of trace gases in the troposphere. *Phys. Chem. Chem. Phys.* **1**, 5401–5408 (1999).
- Intergovernmental Panel on Climate Change, *Climate Change 2013: The Physical Science Basis. Contribution of Working Group I to the Fifth Assessment Report of the Intergovernmental Panel on Climate Change*, T. F. Stocker et al., Eds. (Cambridge University Press, Cambridge, UK, 2013).
- H. Levy II, Normal atmosphere: Large radical and formaldehyde concentrations predicted. *Science* **173**, 141–143 (1971).
- J. A. Logan, M. J. Prather, S. C. Wofsy, M. B. McElroy, Tropospheric chemistry: A global perspective. *J. Geophys. Res.* **86**, 7210–7254 (1981).
- C. M. Spivakovsky et al., Three-dimensional climatological distribution of tropospheric OH: Update and evaluation. *J. Geophys. Res.* **105**, 8931–8980 (2000).
- V. Naik et al., Preindustrial to present-day changes in tropospheric hydroxyl radical and methane lifetime from the Atmospheric Chemistry and Climate Model Intercomparison Project (ACCMIP). *Atmos. Chem. Phys.* **13**, 5277–5298 (2013).
- A. Voulgarakis et al., Analysis of present day and future OH and methane lifetime in the ACCMIP simulations. *Atmos. Chem. Phys.* **13**, 2563–2587 (2013).
- J. F. Lamarque et al., The Atmospheric Chemistry and Climate Model Intercomparison Project (ACCMIP): Overview and description of models, simulations and climate diagnostics. *Geosci. Model Dev.* **6**, 179–206 (2013).
- J. F. Lamarque et al., Historical (1850–2000) gridded anthropogenic and biomass burning emissions of reactive gases and aerosols: Methodology and application. *Atmos. Chem. Phys.* **10**, 7017–7039 (2010).
- D. P. van Vuuren et al., The representative concentration pathways: An overview. *Clim. Change* **109**, 5–31 (2011).
- S. A. Montzka et al., Small interannual variability of global atmospheric hydroxyl. *Science* **331**, 67–69 (2011).
- D. Stone, L. K. Whalley, D. E. Heard, Tropospheric OH and HO<sub>2</sub> radicals: Field measurements and model comparisons. *Chem. Soc. Rev.* **41**, 6348–6404 (2012).
- D. T. Shindell et al., Multimodel simulations of carbon monoxide: Comparison with observations and projected near-future changes. *J. Geophys. Res.* **111**, D19306 (2006).
- P. J. Young et al., Pre-industrial to end 21<sup>st</sup> century projections of tropospheric ozone from the Atmospheric Chemistry and Climate Model Intercomparison Project (ACCMIP). *Atmos. Chem. Phys.* **13**, 2063–2090 (2013).
- L. T. Murray et al., Factors controlling variability in the oxidative capacity of the troposphere since the Last Glacial Maximum. *Atmos. Chem. Phys.* **14**, 3589–3622 (2014).
- C. D. Holmes, M. J. Prather, O. A. Søvde, G. Myhre, Future methane, hydroxyl, and their uncertainties: Key climate and emission parameters for future predictions. *Atmos. Chem. Phys.* **13**, 285–302 (2013).
- L. T. Murray, J. A. Logan, D. J. Jacob, Interannual variability in tropical tropospheric ozone and OH: The role of lightning. *J. Geophys. Res.* **118**, 11468–11480 (2013).
- F. Iglesias-Suarez, P. J. Young, O. Wild, Stratospheric ozone change and related climate impacts over 1850–2100 as modelled by the ACCMIP ensemble. *Atmos. Chem. Phys.* **16**, 343–363 (2016).
- B. D. Santer et al., Identification of human-induced changes in atmospheric moisture content. *Proc. Natl. Acad. Sci. U.S.A.* **104**, 15248–15253 (2007).
- L. T. Murray, Lightning NO<sub>x</sub> and impacts on air quality. *Curr. Pollut. Rep.* **2**, 115–133 (2016).
- G. A. Sanadze, Biogenic isoprene (a review). *Russ. J. Plant Physiol.* **51**, 729–741 (2004).
- B. N. Duncan et al., Global budget of CO, 1988–1997: Source estimates and validation with a global model. *J. Geophys. Res.* **112**, D22301 (2007).
- N. M. Donahue, A. L. Robinson, E. R. Trump, I. Riipinen, J. H. Kroll, "Volatility and aging of atmospheric organic aerosol" in *Atmospheric and Aerosol Chemistry*, V. F. McNeill, P. A. Ariya, Eds. (Topics in Current Chemistry, Springer Berlin Heidelberg, Berlin, 2014), vol. 339, pp. 97–143.
- M. Kanakidou et al., Atmospheric fluxes of organic N and P to the global ocean. *Global Biogeochem. Cycles* **26**, GB3026 (2012).
- P. M. Edwards, M. J. Evans, A new diagnostic for tropospheric ozone production. *Atmos. Chem. Phys.* **17**, 13669–13680 (2017).
- S. A. Safieddine, C. L. Heald, B. H. Henderson, The global nonmethane reactive organic carbon budget: A modeling perspective. *Geophys. Res. Lett.* **44**, 3897–3906 (2017).
- P. O. Wennberg et al., Gas-phase reactions of isoprene and its major oxidation products. *Chem. Rev.* **118**, 3337–3390 (2018).
- M. E. Jenkin, J. C. Young, A. R. Rickard, The MCM v3.3.1 degradation scheme for isoprene. *Atmos. Chem. Phys.* **15**, 11433–11459 (2015).
- D. T. Shindell, G. Faluvegi, N. Bell, Preindustrial-to-present-day radiative forcing by tropospheric ozone from improved simulations with the GISS chemistry-climate GCM. *Atmos. Chem. Phys.* **3**, 1675–1702 (2003).
- F. J. Dentener, P. J. Crutzen, Reaction of N<sub>2</sub>O<sub>5</sub> on tropospheric aerosols—Impact on the global distributions of NO<sub>x</sub>, O<sub>3</sub>, and OH. *J. Geophys. Res.* **98**, 7149–7163 (1993).
- M. J. Evans, D. J. Jacob, Impact of new laboratory studies of N<sub>2</sub>O<sub>5</sub> hydrolysis on global model budgets of tropospheric nitrogen oxides, ozone, and OH. *Geophys. Res. Lett.* **32**, L09813 (2005).
- H. L. Macintyre, M. J. Evans, Sensitivity of a global model to the uptake of N<sub>2</sub>O<sub>5</sub> by tropospheric aerosol. *Atmos. Chem. Phys.* **10**, 7409–7414 (2010).
- H. L. Macintyre, M. J. Evans, Parameterisation and impact of aerosol uptake of HO<sub>2</sub> on a global tropospheric model. *Atmos. Chem. Phys.* **11**, 10965–10974 (2011).
- S. E. Bauer, D. M. Koch, Impact of heterogeneous sulfate formation at mineral dust surfaces on aerosol loads and radiative forcing in the Goddard Institute for Space Studies general circulation model. *J. Geophys. Res.* **110**, D17202 (2005).
- P. S. Romer et al., The lifetime of nitrogen oxides in an isoprene-dominated forest. *Atmos. Chem. Phys.* **16**, 7623–7637 (2016).
- L. W. Horowitz et al., Observational constraints on the chemistry of isoprene nitrates over the eastern United States. *J. Geophys. Res.* **112**, D12508 (2007).
- S. C. Wofsy et al., ATom: Merged atmospheric chemistry, trace gases, and aerosols. [https://daac.ornl.gov/ATOM/guides/ATOM\\_merge.html](https://daac.ornl.gov/ATOM/guides/ATOM_merge.html). Accessed 18 August 2021.
- J. G. John, V. Naik, L. W. Horowitz, J. P. Dunne, Climate versus emission drivers of methane lifetime against loss by tropospheric OH from 1860–2100. *Atmos. Chem. Phys.* **12**, 12021–12036 (2012).
- S. P. Sander et al., "Chemical kinetics and photochemical data for use in atmospheric studies" (JPL Publication 19-5, NASA Jet Propulsion Laboratory, California Institute of Technology, Pasadena, CA, 2006).
- M. M. Rienecker et al., MERRA: NASA's modern-era retrospective analysis for research and applications. *J. Clim.* **24**, 3624–3648 (2011).

## Supplementary Information for

### Uncertainties in global hydroxyl projections tied to fate of reactive nitrogen and carbon

Lee T. Murray, Arlene M. Fiore, Drew T. Shindell, Vaishali Naik, Larry W. Horowitz

Lee T. Murray.

E-mail: [lee.murray@rochester.edu](mailto:lee.murray@rochester.edu)

#### This PDF file includes:

Supplementary text

Figs. S1 to S9

References for SI reference citations

## Supporting Information Text

### S1. Derivation of the steady-state relationship

Here, we derive a solution of the steady-state system of fundamental OH chemistry to relate changes in simulated global mean OH to a simple function of four convolved key parameters: ozone photolysis rates, water vapor abundances, and emissions of reactive nitrogen and carbon species. This relationship was previously applied by Murray et al. (1), and is an expansion of an earlier derivation by Wang and Jacob (2). Figure S1 shows the coupling between the dominant reactions and species that influence OH abundances.

The primary source of HO<sub>x</sub> (≡ OH + peroxy) radicals to the troposphere is the photolysis of ozone to O(<sup>1</sup>D), followed by reaction with water vapor,



otherwise, O(<sup>1</sup>D) is quenched and reforms ozone,



Cycling of HO<sub>x</sub> species during oxidation of CO in the presence of NO<sub>x</sub> (≡ NO + NO<sub>2</sub>) leads to ozone production,



In addition to R5, the oxidation of NO to NO<sub>2</sub> also takes place by reaction with ozone,



Loss of HO<sub>x</sub> radicals is primarily by self-reaction of HO<sub>2</sub> and by oxidation of NO<sub>2</sub> by OH to nitric acid,



Ozone is also transported from the stratosphere and can be lost by deposition to the surface.

The steady state equations of the system described by reactions R1 through R9 for HO<sub>x</sub>, OH, O<sub>3</sub>, NO<sub>x</sub>, and CO concentrations are, respectively,

$$2 \frac{J_{\text{R1}} k_{\text{R2}} [\text{H}_2\text{O}]}{k_{\text{R3}} [\text{M}]} [\text{O}_3] = 2k_{\text{R8}} [\text{HO}_2]^2 + k_{\text{R9}} [\text{OH}] [\text{NO}_2] [\text{M}] \quad [1]$$

$$k_{\text{R5}} [\text{HO}_2] [\text{NO}] + 2 \frac{J_{\text{R1}} k_{\text{R2}} [\text{H}_2\text{O}]}{k_{\text{R3}} [\text{M}]} [\text{O}_3] = k_{\text{R4}} [\text{OH}] [\text{CO}] + k_{\text{R9}} [\text{OH}] [\text{NO}_2] [\text{M}] \quad [2]$$

$$k_{\text{R5}} [\text{HO}_2] [\text{NO}] + F_{\text{STE}} = \frac{J_{\text{R1}} k_{\text{R2}} [\text{H}_2\text{O}]}{k_{\text{R3}} [\text{M}]} [\text{O}_3] + k_d [\text{O}_3] \quad [3]$$

$$S_N = L_N = k_{\text{R9}} [\text{OH}] [\text{NO}_2] [\text{M}] \quad [4]$$

$$S_C = L_C = k_{\text{R4}} [\text{OH}] [\text{CO}] \quad [5]$$

where  $k_i$  or  $J_i$  is the reaction or photolysis rate constant for reaction  $i$ ,  $k_d$  is the ozone depositional loss frequency ( $\text{s}^{-1}$ ),  $F_{\text{STE}}$  is the net transport rate of ozone from the stratosphere to the troposphere ( $\text{molecules cm}^{-3} \text{ s}^{-1}$ ), and  $S_N$  and  $S_C$  are the source rates of NO<sub>x</sub> and CO, respectively ( $\text{molecules cm}^{-3} \text{ s}^{-1}$ ). Note that the rate-limiting step for ozone production is formation of NO<sub>2</sub> from NO+HO<sub>2</sub>. We further assume that the loss of NO<sub>x</sub> ( $L_N$ ) and reactive carbon ( $L_C$ ) occur only through reactions R9 and R4, respectively.

To derive the dependence of OH, first we assume O<sub>3</sub>-NO-NO<sub>2</sub> photochemical steady state (photostationary assumption) from reactions (R6 -R7), i.e.

$$J_{\text{R6}} [\text{NO}_2] = k_{\text{R7}} [\text{NO}] [\text{O}_3] \quad [6]$$

We combine equation 6 with equations 1–5, and explicitly solve the linear set of equations to obtain

$$[\text{OH}] = \left( \frac{J_{\text{R6}} k_{\text{R5}} S_N (3[\text{H}_2\text{O}] J_{\text{R1}} k_{\text{R2}} + k_{\text{R3}} k_d [\text{M}])^{3/2}}{\sqrt{2} k_{\text{R3}} k_{\text{R7}} k_{\text{R9}} [\text{M}]^2 (S_C + S_N + F_{\text{STE}})} \right) \times \sqrt{\frac{[\text{H}_2\text{O}] J_{\text{R1}} k_{\text{R2}} (2S_C - S_N + 2F_{\text{STE}}) - k_{\text{R3}} k_d [\text{M}] S_N}{k_{\text{R8}} ([\text{H}_2\text{O}] J_{\text{R1}} k_{\text{R2}} (S_C + S_N - 2F_{\text{STE}}) + k_{\text{R3}} k_d [\text{M}] (S_C + S_N))^2}} \quad [7]$$

Using typical tropospheric concentrations, rate constants and fluxes to identify negligible terms, eq. 7 may be reduced to a functional form of

$$[\text{OH}] \propto \kappa J_{\text{O}(^1D)}[\text{H}_2\text{O}] \frac{S_N}{S_C^{3/2}} \quad [8]$$

where  $J_{\text{O}(^1D)} \equiv J_{\text{R1}}$  is the mass-weighted mean tropospheric photolysis frequency for ozone to  $\text{O}(^1D)$  ( $\text{s}^{-1}$ ),  $[\text{H}_2\text{O}]$  is the mean tropospheric water vapor concentration (molecules  $\text{cm}^{-3}$ ),  $S_N$  is the total  $\text{NO}_x$  emission rate ( $\text{mol N cm}^{-3} \text{s}^{-1}$ ), and  $S_C$  is the total reduced carbon species emission rate ( $\text{mol C cm}^{-3} \text{s}^{-1}$ ), and  $\kappa$  is an effective constant that reflects the relative weighting of the second and higher-order terms. Wang et al. (2) were the first to use a similar derivation to relate the changes in global mean  $[\text{OH}]$  to  $S_N/S_C^{3/2}$ , in order to describe behavior of simulated OH with and without anthropogenic emissions. Murray et al. (1) later expanded the derivation into Eq. (8) to also include the effects of climate-driven variability in water vapor and overhead ozone abundances.

## S2. Adjustments to the ACCMIP archive

In multi-model inter-comparison studies, native model diagnostics must be converted into standardized fields with common units for analysis, and are therefore susceptible to definitional and unit-conversion errors. For example, *eminox* is meant to include all anthropogenic and natural  $\text{NO}_x$  sources in units of  $\text{kg N m}^{-2} \text{s}^{-1}$ ; however, many models archived only anthropogenic  $\text{NO}_x$  and/or in units of  $\text{kg NO m}^{-2} \text{s}^{-1}$ . We have evaluated each archived variable against reasonable physical limits and the self-reported values in the supplemental materials of the ACCMIP overview paper (3). Assumptions made to adjust the archived values to match the requested units and variable fields or disclude fields from our analysis are outlined below.

**CESM-CAM-superfast.** Ozone photolysis frequencies (*photo1d*) were not archived for this model. Instead, we derive them from the production rate of OH from ozone photolysis (*prodohjo3*),

$$J_{\text{O}(^1D)} = P(\text{OH}) \cdot \frac{3.3 \times 10^{-11} \exp\left(\frac{55}{T}\right) [\text{O}_2] + 2.15 \times 10^{-11} \exp\left(\frac{110}{T}\right) [\text{N}_2]}{2 \left(1.63 \times 10^{-10} \exp\left(\frac{60}{T}\right)\right) [\text{H}_2\text{O}][\text{O}_3]},$$

where  $P(\text{OH})$  is *prodohjo3* converted to molecules  $\text{cm}^{-3} \text{s}^{-1}$ ,  $T$  is the local absolute temperature in K,  $[\text{N}_2]$ ,  $[\text{O}_2]$  and  $[\text{H}_2\text{O}]$  are respectively the number densities of oxygen, nitrogen and water vapor in molecules  $\text{cm}^{-3}$  determined using archived temperature, pressure and mixing ratios, and the rate constants are taken from the JPL 2011 recommendations (4).

In order to match the emissions reported by Lamarque et al. (3): we consider *eminox* to be actually archived as  $\text{kg NO m}^{-2} \text{s}^{-1}$  and without lightning  $\text{NO}_x$  or a constant  $2.8 \text{ Tg N yr}^{-1}$  of other natural sources, and for *emivoc* to be actually archived as  $\text{kg isoprene m}^{-2} \text{s}^{-1}$ .

**CICERO-OsloCTM2.** In order to match the emissions reported by Lamarque et al. (3), we consider all archived emissions to not include any natural sources. In this study, we add the constant natural emission fluxes reported for these simulations by Skeie et al. (5):  $5 \text{ Tg N yr}^{-1}$  of lightning  $\text{NO}_x$  and  $8 \text{ Tg N yr}^{-1}$  of other natural  $\text{NO}_x$ ,  $180 \text{ Tg yr}^{-1}$  of biogenic CO, and  $397 \text{ Tg C yr}^{-1}$  of biogenic NMVOCs.

**CMAM.** Emissions of NMVOCs are zero in this model. The chemical loss of CO for several years of the RCP 8.5 scenario is many orders of magnitude too high, and these years are discluded from this analysis.

**EMAC.** In order to match the emissions reported by Lamarque et al. (3): *eminox* is considered to be actually archived as  $\text{kg NO m}^{-2} \text{s}^{-1}$ , and *emivoc* is scaled by the mass ratio of C to total mass of NMVOC assumed by the model (161/210) (6). RCP 8.5 is not included in this analysis due to non-physical archived model air masses.

**GEOSCCM.** All variables used in this study are correctly archived.

**GFDL-AM3.** Archived *eminox* did not include lightning  $\text{NO}_x$ , which we add in this analysis.

**GISS-E2-R.** All variables used in this study are correctly archived.

**GISS-E2-TOMAS.** In order to match the emissions reported by Lamarque et al. (3), *emivoc* is multiplied by the molar mass ratio of isoprene in grams (68).

**HadGEM2.** In order to match the emissions reported by Lamarque et al. (3), *eminox* is considered to be actually archived as  $\text{kg NO}_2 \text{ m}^{-2} \text{s}^{-1}$  and without lightning  $\text{NO}_x$ . One year of RCP 8.5 is not included in this analysis due to error in model level height precluding airmass calculation.

**LMDzORINCA.** Historical emissions of CO or NMVOC were not archived, so decadal mean *emico* and *emivoc* are prescribed from the values reported in Lamarque et al. (3) in this scenario.

**MIROC-CHEM.** In order to match the emissions reported by Lamarque et al. (3), *eminox* is considered to be actually archived as  $\text{kg NO}_2 \text{ m}^{-2} \text{s}^{-1}$  and without lightning  $\text{NO}_x$ . Lightning emissions were not archived, so decadal mean *emilnox* is prescribed from the values reported in Lamarque et al. (3).

**MOCAGE.** In order to match the emissions reported by Lamarque et al. (3), *eminox* is considered to be actually archived as  $\text{g N m}^{-2} \text{ s}^{-1}$ , and *emico* and *emivoc* are considered to be actually archived as  $\text{g C m}^{-2} \text{ s}^{-1}$ . Lightning emissions in 1983 and 2003 of the historical scenario and 2032 of the RCP 8.5 scenario are unrealistic, and not included in this analysis.

**NCAR-CAM3.5.** In order to match the emissions reported by Lamarque et al. (3), *eminox* is considered to be actually archived without lightning  $\text{NO}_x$ . The *emivoc* field was not archived, so decadal mean values reported by Lamarque et al. (3) are used instead. The chemical loss rates of CO (*lossco*) and methane (*lossch4*) were treated as if they were archived as  $\text{molecules cm}^{-3} \text{ s}^{-1}$ , and *lossch4* was scaled by an additional factor of 0.01 for all scenarios except RCP 6.0.

**STOC-HadAM3.** All variables used in this study are correctly archived.

**UM-CAM.** All variables used in this study are correctly archived.

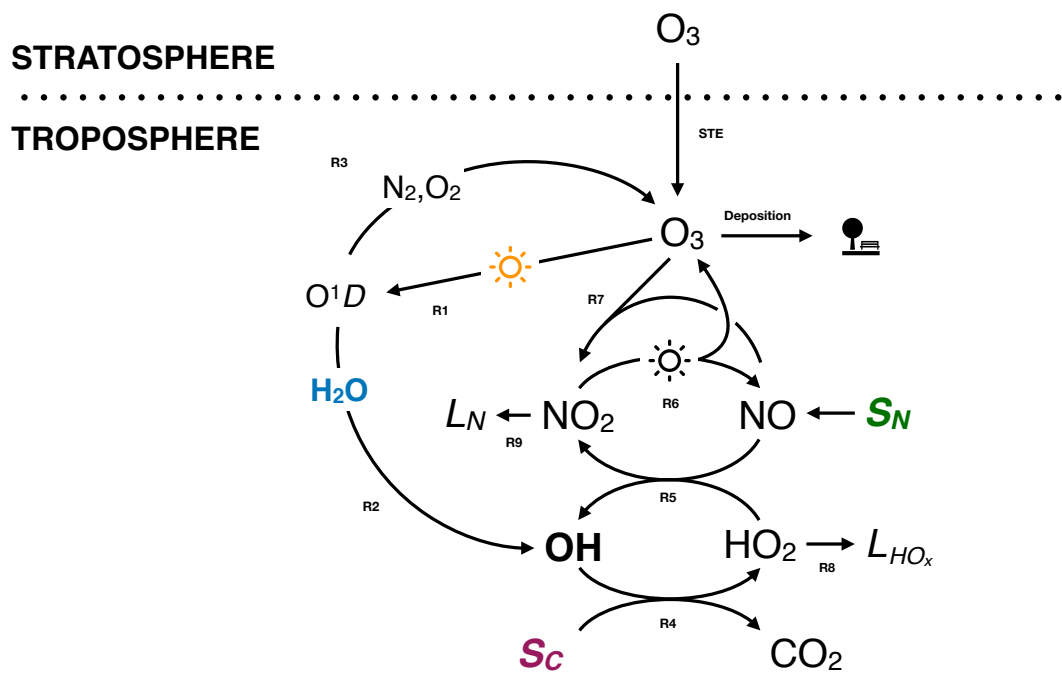
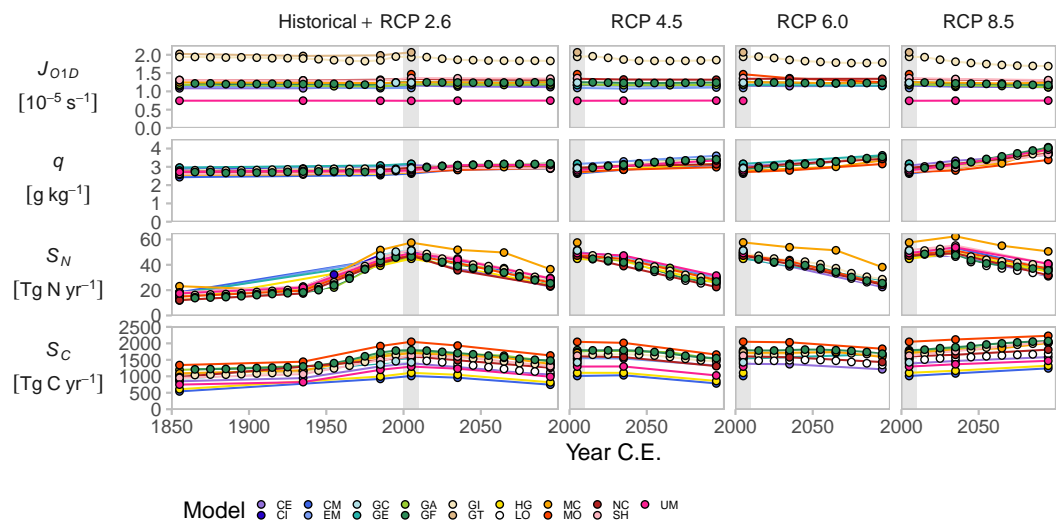
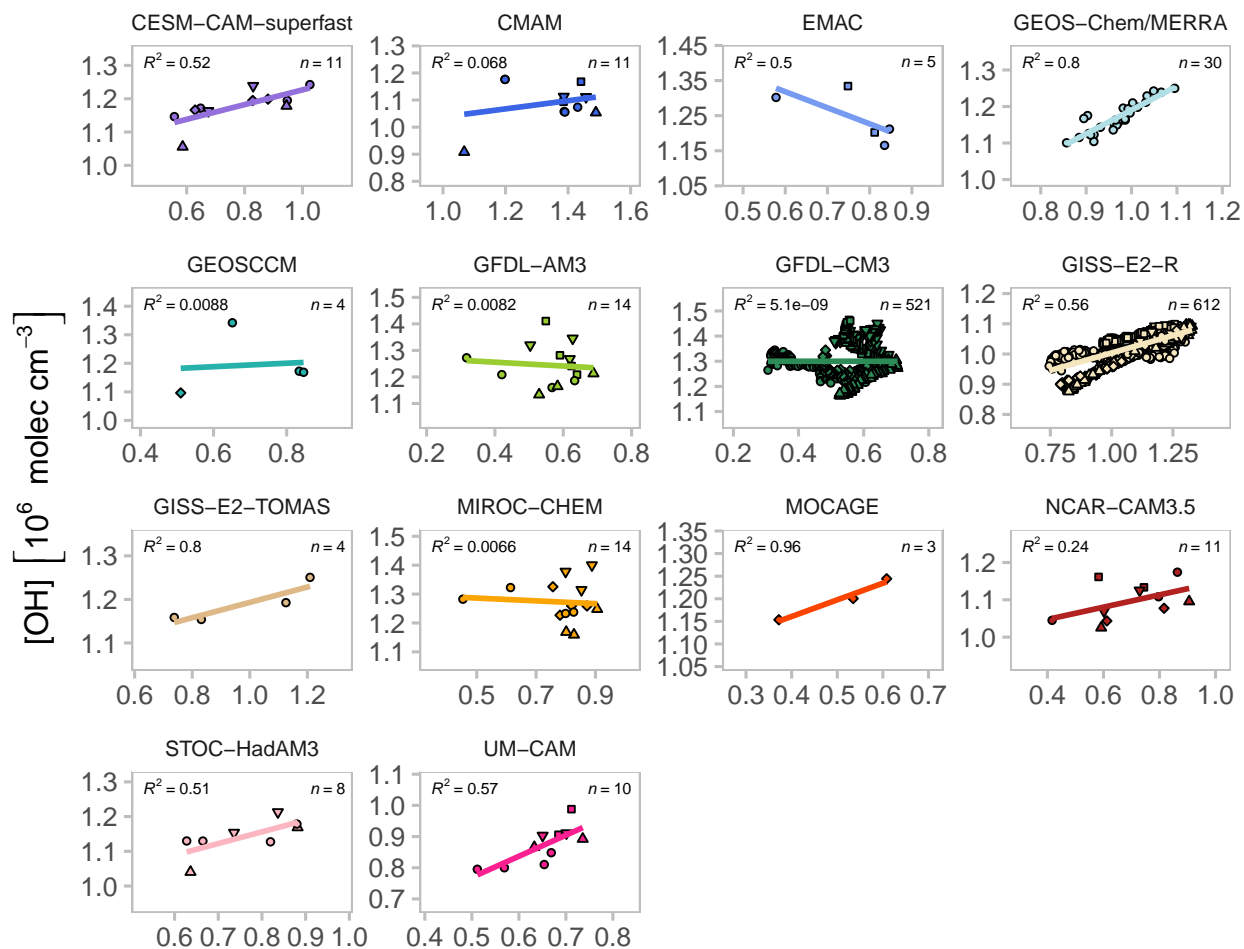


Fig. S1. Diagram of dominant chemical reactions affecting OH. The four key parameters of Eq. [1] are highlighted in colors.



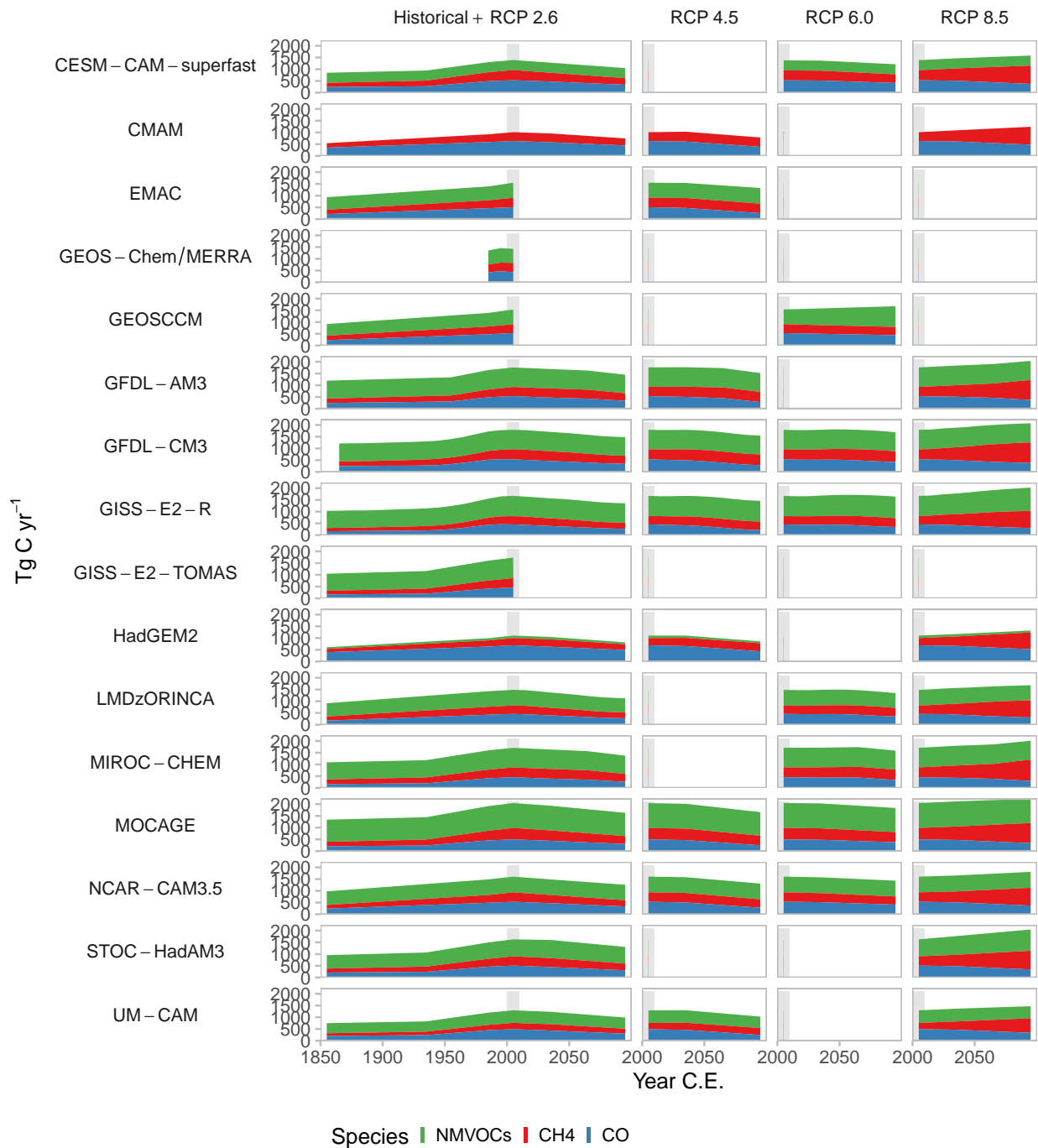
**Fig. S2.** Key parameters for OH photochemistry exhibit large temporal and inter-model variability in the ACCMIP simulations. *Top row:* Tropospheric mass-weighted mean decadal photolysis frequency of ozone to  $O(^1D)$  in  $10^5 \text{ s}^{-1}$ . *Second row:* Tropospheric decadal mean water vapor abundance in  $\text{g H}_2\text{O}$  per  $\text{kg air}$ . *Third row:* Decadal mean reactive nitrogen source in  $\text{Tg N yr}^{-1}$ . *Bottom row:* Decadal mean total reactive carbon source in  $\text{Tg C yr}^{-1}$ . Not all simulations submitted all variables for all experiments.



$$J_{O1D} q \left( \frac{S_N}{S_C^{3/2}} \right) \left[ 10^{-7} \text{ s}^{-1} \text{ g kg}^{-1} \left\{ \frac{\text{Tmol}}{\text{yr}} \right\}^{-1/2} \right]$$

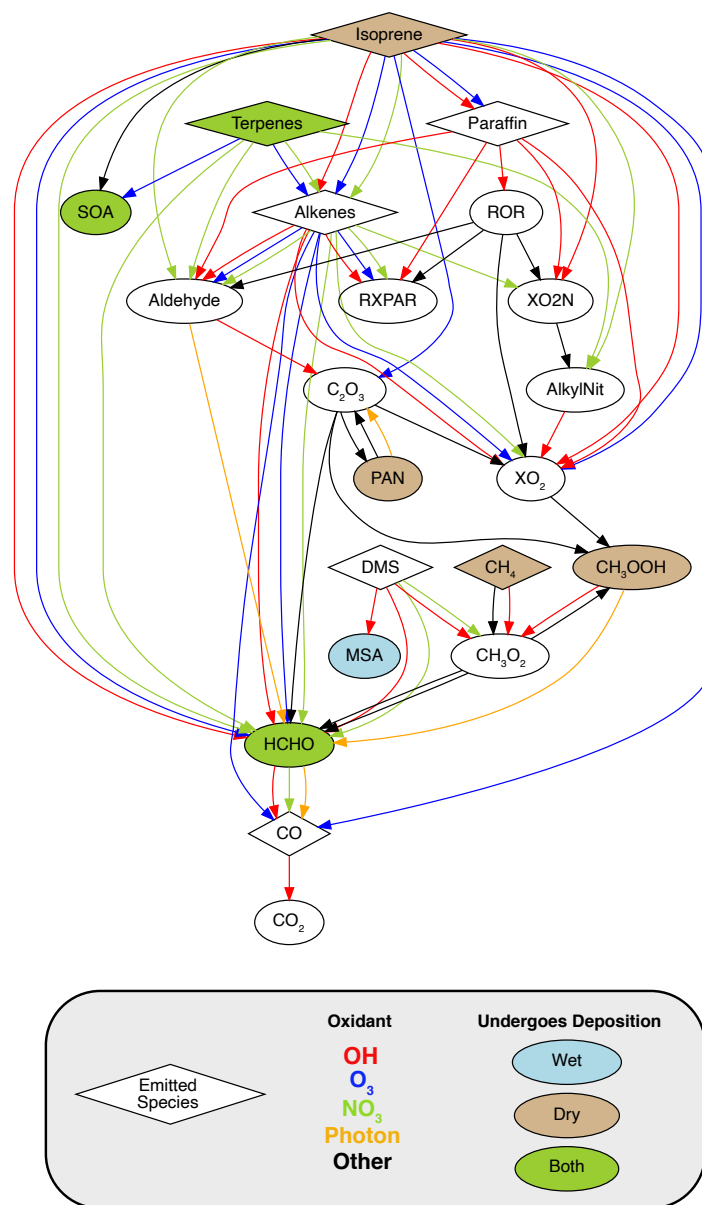


Fig. S3. Same as Fig. 2 in the main text, but with each model that contributed all four key parameters isolated, and showing annual means rather than decadal means.



**Fig. S4.** Reactive carbon emission time series broken down by type. Stacked area charts indicate the magnitude of  $S_C$  associated with CO (blue), methane (red), and NMVOCs (green). Each row shows the time series for a different model.

## GISS-E2-R Hydrocarbon Oxidation Mechanism



**Fig. S5.** Flow chart from emission to removal of reactive carbon species in the GISS-E2-R oxidation mechanism as described by Shindell et al. (7–10). Emitted reduced carbon species shown as diamonds. Chemical reactions are represented as directional arrows colored by oxidant (red = OH; blue = ozone; green = nitrate radical; orange = photolysis; black = other). Species that may be removed from the atmosphere via wet or dry deposition processes are shaded as light blue or tan, respectively. Those that may be removed by either are shaded as green.



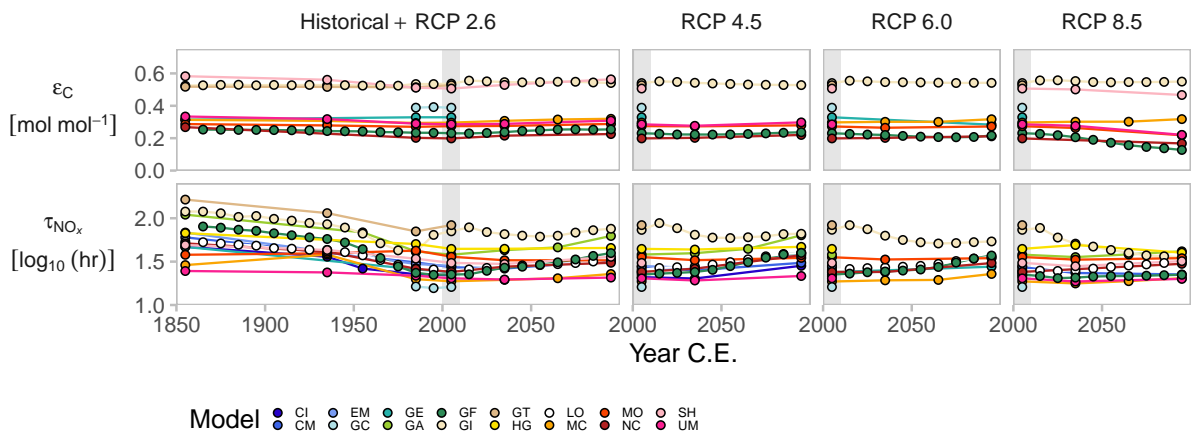


**Fig. S7.** Decadal mean oxidative efficiency ( $\epsilon_{\text{ox}}$ ; top row; unitless) and the  $\log_{10}$ -transformed decadal mean  $\text{NO}_x$  lifetime ( $\tau_{\text{NO}_x}$ ; bottom row;  $\log_{10}$ (hr)) in the ACCMIP simulations.

$\text{NO}_y \equiv \text{NO}_x + \text{Reservoir Species}$

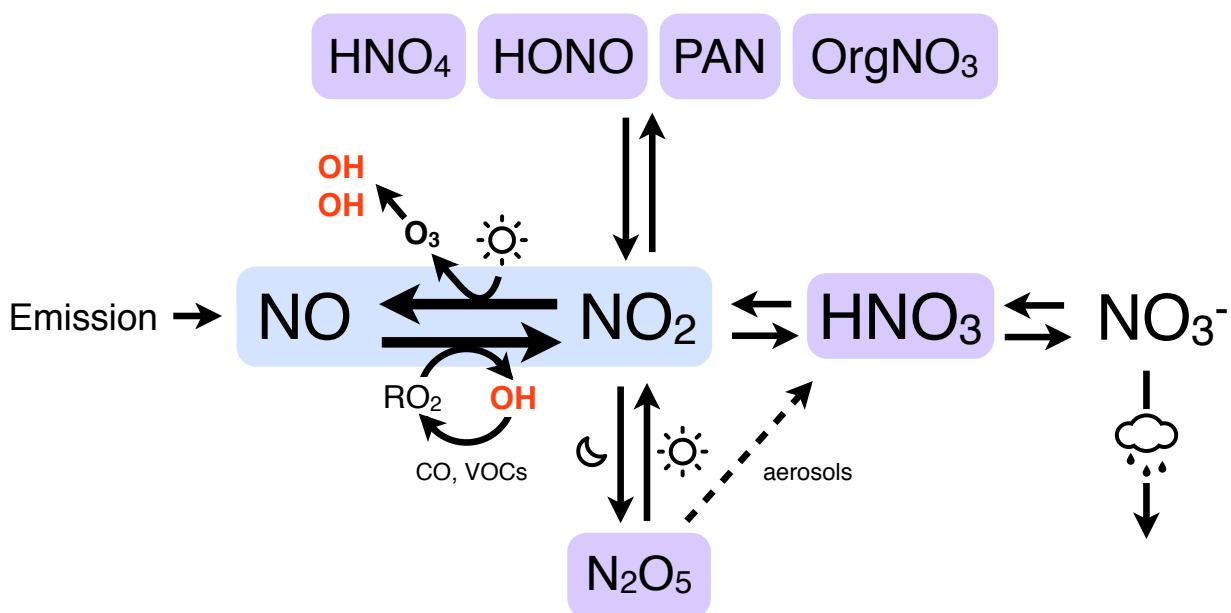


Fig. S8. Schematic of the tropospheric reactive nitrogen budget.

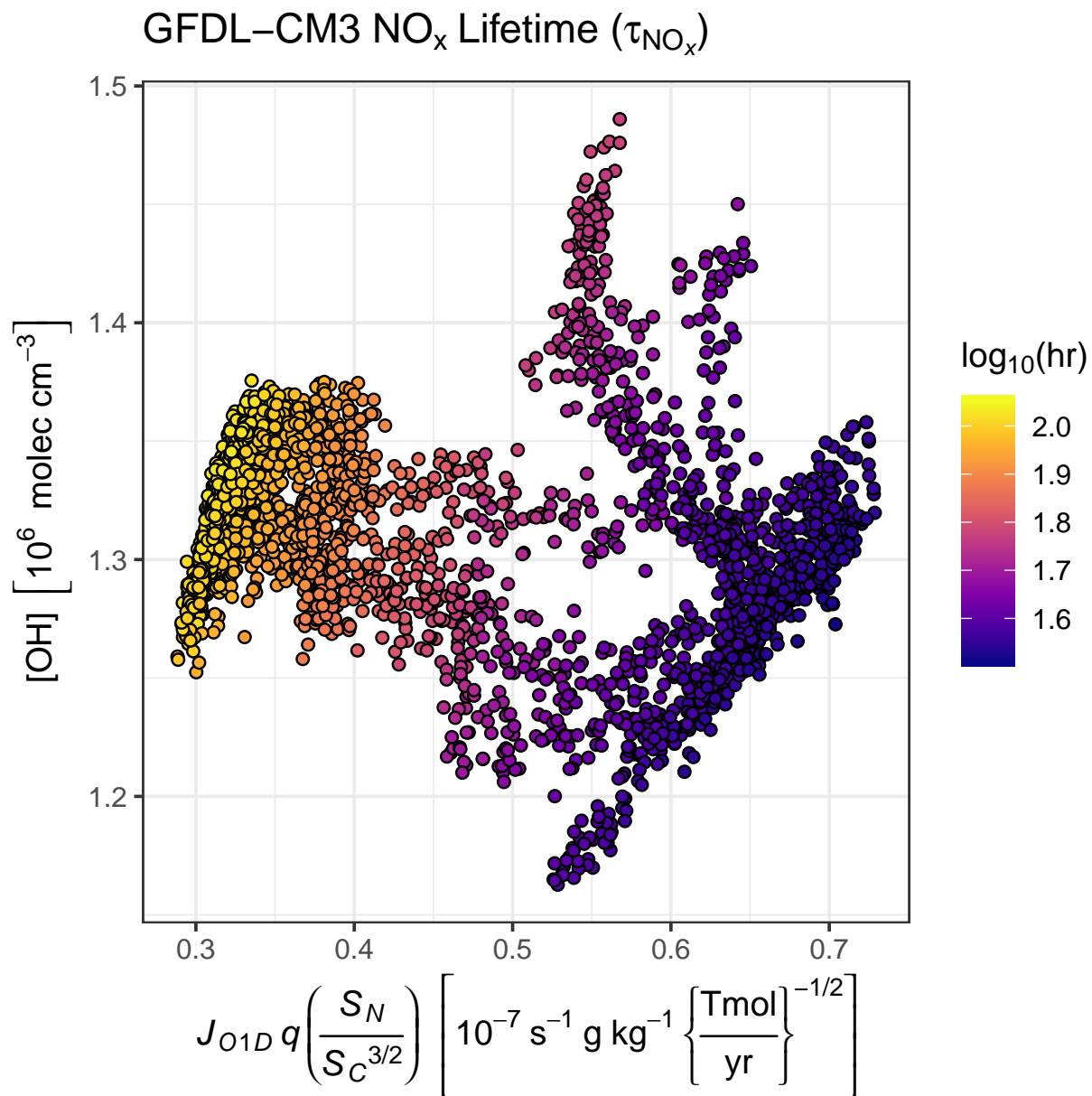


Fig. S9. Annual mean tropospheric NO<sub>x</sub> lifetime in log<sub>10</sub>(hr) of the entire ensemble of GFDL-CM3 simulations contributed to CMIP5, of which the ACCMIP runs are a subset.

## References

1. Murray LT, et al. (2014) Factors controlling variability in the oxidative capacity of the troposphere since the Last Glacial Maximum. *Atmos Chem Phys* 14(7):3589–3622.
2. Wang YH, Jacob DJ (1998) Anthropogenic forcing on tropospheric ozone and OH since preindustrial times. *J Geophys Res Atmos* 103(D23):31123–31135.
3. Lamarque JF, et al. (2013) The Atmospheric Chemistry and Climate Model Intercomparison Project (ACCMIP): overview and description of models, simulations and climate diagnostics. *Geosci Model Dev* 6(1):179–206.
4. Sander SP, et al. (2011) *Chemical Kinetics and Photochemical Data for Use in Atmospheric Studies*. (JPL Publication 10-6).
5. Skeie RB, et al. (2011) Anthropogenic radiative forcing time series from pre-industrial times until 2010. *Atmos Chem Phys* 11(22):11827–11857.
6. Klinger C (2011) Master's thesis (Faculty of Physics, Meteorological Institute Munich).
7. Shindell DT, Grenfell JL, Rind DH, Grewe V, Price CG (2001) Chemistry-climate interactions in the Goddard Institute for Space Studies general circulation model: 1. Tropospheric chemistry model description and evaluation. *J Geophys Res* 106(D8):8047.
8. Shindell DT, Faluvegi G, Bell N (2003) Preindustrial-to-present-day radiative forcing by tropospheric ozone from improved simulations with the GISS chemistry-climate GCM. *Atmos Chem Phys* 3(5):1675–1702.
9. Shindell DT, et al. (2006) Simulations of preindustrial, present-day, and 2100 conditions in the NASA GISS composition and climate model G-PUCCINI. *Atmos Chem Phys* 6(12):4427–4459.
10. Shindell DT, et al. (2013) Interactive ozone and methane chemistry in GISS-E2 historical and future climate simulations. *Atmos Chem Phys* 13(5):2653–2689.
11. Horowitz LW, et al. (2003) A global simulation of tropospheric ozone and related tracers: Description and evaluation of MOZART, version 2. *J Geophys Res* 108(D24):4784.
12. Horowitz LW, et al. (2007) Observational constraints on the chemistry of isoprene nitrates over the eastern United States. *J Geophys Res* 112(D12):955.